Journal of Materials Chemistry A

Operando Investigation of Aqueous Zinc Manganese Oxide Batteries: Multi-Stage Reaction Mechanism Revealed

Journal:	*Journal of Materials Chemistry A*
Manuscript ID	TA-ART-03-2023-001549.R1
Article Type:	Paper
Date Submitted by the Author:	28-May-2023
Complete List of Authors:	Wu, Daren; Stony Brook University, Materials Science and Chemical Engineering King, Steven; Stony Brook University, Chemistry Sadique, Nahian; Stony Brook University, Chemistry Ma, Lu; Brookhaven National Laboratory, National Synchrotron Light Source II Ehrlich, Steven; Brookhaven national lab., Ghose, Sanjit; Brookhaven National Laboratory, National Synchrotron Light Source II Bai, Jianming; Brookhaven National Lab, Zhong, Hui; Stony Brook University, Yan, Shan; Brookhaven National Laboratory, Bock, David; Brookhaven National Laboratory, Takeuchi, Esther; Stony Brook University, Materials Science and Engineering Marschilok, Amy; Stony Brook University, Materials Science and Engineering Housel, Lisa; Brookhaven National Laboratory Wang, Lei; Brookhaven National Laboratory, Energy and Photon Science Takeuchi, Kenneth; Stony Brook University, Chemistry

ARTICLE

Operando Investigation of Aqueous Zinc Manganese Oxide Batteries: Multi-Stage Reaction Mechanism Revealed

Received 00th January 20xx,
Accepted 00th January 20xx

DOI: 10.1039/x0xx00000x

Daren Wu,[a,b] Steven T. King, [a,c] Nahian Sadique,[a,c] Lu Ma,[d] Steven N. Ehrlich,[d] Sanjit Ghose,[d] Jianming Bai,[d] Hui Zhong,[d], Shan Yan,[a,e] David C. Bock,[a,e] Esther S. Takeuchi,[a,b,c,e] Amy C. Marschilok,[a,b,c,e] Lisa M. Housel,[a,e] Lei Wang,[a,e] Kenneth J. Takeuchi*[a,b,c,e]

Aqueous Zn/MnO_2 batteries with mildly acidic electrolytes are promising candidates for low cost, high safety electrochemical energy storage for grid-scale applications. However, the complexity of the chemistry results in conflicting reports of operation principles, making rational improvements challenging. In this work, *operando* synchrotron X-ray diffraction (XRD) and X-ray absorption spectroscopy (XAS) as well as *ex-situ* Raman spectroscopy, XRD, and XAS characterization were used to probe the mechanism of aqueous Zn/α-MnO_2 batteries with $ZnSO_4$ electrolyte. A multi-stage Mn dissolution-conversion charge storage mechanism was revealed, which consists of reversible solid-aqueous phase transformation *via* Mn dissolution-deposition reactions and solid redox mechanism via Zn-ion insertion. This mechanism is supported by thermodynamic calculations paired with *in-situ* electrolyte pH measurements to provide further mechanistic insights. The findings establish a detailed charge storage mechanism for aqueous Zn/α-MnO_2 batteries with well resolved reversible layered charge product structure, that can serve as a reference for future studies on advancing the reversibility and stability of aqueous Zn/α-MnO_2 batteries.

Introduction

High-energy, long-lasting, and cost-effective energy storage is paramount for widespread use of intermittent renewable energy sources in the electric grid. Electrochemical energy storage (EES) solutions are versatile with applications in energy arbitrage, generation capacity deferral, ancillary services, ramping, transmission and distribution capacity deferral, and end-user applications, where batteries can be deployed in the electricity grid for short-term and long-term energy delivery. Li-ion batteries (LIBs) are currently most common, accounting for 768 MW of deployed EES grid energy storage in the U.S. However, inherent safety and cost of the systems raise concern.[1-3] As an alternative, aqueous Zn-ion batteries (AZIB) can offer superior safety by eliminating flammable electrolytes with added advantages of using Zn metal including low cost, high natural abundance, and scalable processing.[3-7] Commercialization of AZIB technologies requires compatible cathodes that can operate within the water stability window, are reversible, and have long cycle life.

Manganese oxides have the environmental benefits, appropriate voltage window and high natural abundance attractive for AZIB cathodes. Furthermore, manganese oxides demonstrate structural versatility, providing a broad material class for exploration.[8-9] α-MnO_2 is among the most studied, as its 2×2 MnO_6 octahedral tunneled framework provides the benefit of void space for ion insertion with structural robustness. Electrochemical reversibility of Zn/α-MnO_2 cells can be achieved by using mildly acidic electrolyte such as $ZnSO_4$.[4, 6, 10-14] Zn/α-MnO_2 cells with $ZnSO_4$ electrolyte have been reported to operate primarily via H^+ or Zn^{2+} (co)insertion.[4, 12, 15-21] *Ex-situ* x-ray diffraction (XRD) and bright-field transmission electron microscopy (TEM) suggested Zn^{2+} insertion into α-MnO_2 tunnels resulting in reversible rearrangement to spinel $ZnMn_2O_4$ or layered Zn_xMnO_2 phases.[12, 15, 22] Proton conversion mechanisms were proposed based on high resolution TEM evidence, where H^+ ions reacted with MnO_2 to form MnOOH, while OH^- ions react with $ZnSO_4$ and H_2O to form zinc hydroxy-sulfate (ZHS) precipitates.[10, 20]

More recently, Zn/α-MnO_2 cells with mildly acidic electrolytes were shown to operate via a Faradaic Mn dissolution-deposition process.[23-34] In particular, *operando* Mn K-edge X-ray fluorescence maps and Extended X-ray Absorption Fine Structure (EXAFS) probing enabled visualization, speciation and quantification of Mn^{n+} species that form in the electrolyte during discharge and deplete on charge in Zn/α-MnO_2 cell with

[a.] *Institute of Energy: Sustainability, Environment, and Equity, Stony Brook University, Stony Brook, New York 11794, USA.*
[b.] *Department of Materials Science and Chemical Engineering, Stony Brook University, Stony Brook, New York 11794, USA.*
[c.] *Department of Chemistry, Stony Brook University, Stony Brook, New York 11794, USA.*
[d.] *National Synchrotron Light Source II, Brookhaven National Laboratory, Upton, New York 11973, USA.*
[e.] *Interdisciplinary Science Department, Brookhaven National Laboratory, Upton, New York 11973, USA.*
*Corresponding author: kenneth.takeuchi.1@stonybrook.edu

Electronic Supplementary Information (ESI) available: [details of any supplementary information available should be included here]. See DOI: 10.1039/x0xx00000x

different mildly acidic electrolytes, providing direct evidence of the Mn dissolution-deposition mechanism.[30, 34] Complementary TEM and XRD evidence demonstrated that Mn dissolution coincides with formation of a crystalline zinc hydroxy byproduct.[29, 35] Variations in electrolyte pH as a result of Faradaic Mn^{n+} dissolution-deposition were observed via *operando* pH measurements[32-33] and local pH tuning, via electrolyte modification and self-buffering aimed at enhancing dissolution-deposition efficiency was demonstrated.[36-38] Different reaction stages of Mn dissolution/deposition mechanism were recently proposed and probed using an electrochemical quartz-crystal microbalance (EQCM).[26] Further, the dissolution-deposition mechanism has been noted in Zn/MnO_2 systems with several different electrolytes[29, 39] and MnO_2 cells with Cu, Bi, and Zn anodes.[40] Additionally, the dissolution-deposition mechanism has been suggested for other MnO_2 polymorphs such as δ-MnO_2[41], β-MnO_2[42-43], and electrolytic manganese oxides (EMD).[44-47]

With cathode Mn dissolution-deposition mechanism well demonstrated and proved, a deeper understanding of different reaction stages manifest in the multiple voltage plateaus during cycling is needed for the next step optimization of AZIBs. In this work, complimentary *operando* X-ray diffraction and X-ray absorption spectroscopy (XAS) measurements demonstrate the structural and chemical changes over different stages of cycling in an aqueous Zn/α-MnO_2 battery (AZMB) with mildly acidic $ZnSO_4$ electrolyte. *Operando* Raman spectroscopy, *operando* optoelectrochemistry, and *ex-situ* extended x-ray fine structure (EXAFS) analysis as well as *in-situ* electrolyte pH measurements establish a multi-stage reaction mechanism. This study deepens the understanding of rechargeable AZIBs dominated by Mn dissolution-deposition mechanism, providing experimental evidence and thermodynamic calculation support for an additional solid-state Zn-ion insertion redox stage that can be assigned to different voltage plateaus demonstrated in the cycling process. With the multiple reaction stages elucidated, optimization, characterization and control of different reaction stages for AZIBs can be systematically improved.

Experimental Methods

Materials synthesis: α-MnO_2 nanofibers were synthesized by adapting a previous reported method.[48] Briefly, $MnSO_4{\cdot}H_2O$, K_2SO_4 and $K_2S_2O_8$ in a molar ratio of 1:1:2 were dissolved in deionized water, transferred to a polymer lined stainless steel autoclave and held at 200°C for 96 h. The resulting product was washed with deionized water and dried under vacuum.

Material Characterization: X-ray diffraction (XRD) of the pristine material was collected at the 28-ID-2 XPD beamline of the National Synchrotron Light Source II (NSLS-II) at Brookhaven National Laboratory (BNL) with a wavelength of 0.1874Å calibrated by a LaB_6 standard and a beam distance of 1.3788 m. Water content was estimated from thermogravimetric analysis (TGA) using a TA instrument SDT Q600 under nitrogen. The K and Mn elemental ratio of the synthesized material was determined from inductively coupled plasma-optical emission spectroscopy (ICP-OES) using a Thermofisher iCap 6300 series instrument.

Electrode preparation and electrochemical measurements: The synthesized α-MnO_2 nanofibers and multi-wall carbon nanotubes (MWCNT) were dispersed in solvent, sonicated in a mass ratio of 7:3, and vacuum-filtered to form a composite electrode. Electrochemical cells were assembled with the α-MnO_2/CNT cathode, glass fiber separator, zinc foil anode, and aqueous 2 M $ZnSO_4$ electrolyte. Galvanostatic cycling tests were conducted using a Maccor testing system or a BioLogic SP-300 potentiostat at a current of 150 mA/g between 1.1 and 1.7 V. Electrodes in charged and discharge states were recovered, rinsed with deionized water and vacuum dried.

X-ray Diffraction Characterization: Post-electrochemistry *ex-situ* XRD was performed using a Rigaku SmartLab diffractometer with Cu Kα radiation and Bragg-Brentano focusing geometry. *Operando* XRD measurements were performed during electrochemical cycling at NSLS-II using the 28-ID-2 XPD beamline with a wavelength of 0.1874Å calibrated by a LaB_6 standard and a beam distance of 1.3788 m. Galvanostatic cycling was performed using a Biologic VSP multichannel potentiostat for two cycles from 1.1 to 1.7V at a current rate of 50 mA/g. XRD patterns were collected at every 10 minutes during cycling. Rietveld refinements were performed using GSASII.[49] A background peak was added near 3.2° to account for the presence of CNT from the composite electrodes. Additionally, Zn and Ti phases were fit to account for the titanium and Zn visible from the cell configuration. Errors for unit cell parameters, phase fractions, crystallite size, preferred orientation, were determined and reported from the GSASII fit results.

X-ray Absorption Spectroscopy Characterization: Mn K-edge x-ray absorption near edge structure (XANES) and extended x-ray absorption fine structure (EXAFS) measurements were collected at 7-BM of the NSLS-II at BNL. All spectra were aligned, merged and normalized using Athena.[50] *Operando* XANES measurements used a custom cell containing the prepared cathode, glass fiber separator, zinc anode and 2 M $ZnSO_4$ electrolyte.

Operando Raman. Operando Raman spectra were recorded on a Horiba Scientific XploRA instrument with a 532 nm laser while the Zn-MnO_2 cell was (dis)charged between 0.2-1.8 V at a current density of 150 mA/g for two cycles. A total of 420 spectra were recorded during the two electrochemical (dis)charge cycles. Optoelectrochemical testing was carried out using with MnO_2 cathode and Zn anode in a 2M $ZnSO_4$ electrolyte. The cell was (dis)charged between 1.1-1.8V at a current density of 150 mA/g for two cycles using a BioLogic potentiostat, while the optical videos of the cells were acquired using an Olympus TH4-100 Microscope. Ex situ Raman spectra of the charge product collected on the carbon current collector after two cycles were collected with 50X objective.

NMF analysis of operando Raman data. Raman spectra were processed using non-negative matrix factorization (NMF) to identify and unmix discrete spectral signal components. Prior to NMF model training, the spectra were preprocessed by cropping the spectral range to 200-725 cm^{-1} to eliminate high

energy bands arising primarily from the electrolyte and carbon nanotube conductive element, cosmic peak outlier removal, and 3rd order polynomial baseline estimation and subtraction. The optimal number of components for NMF decomposition was estimated by first training a principal component analysis (PCA) model on the preprocessed spectra, then using a scree plot of the trained PCA model to determine the approximate number of separable signal components. A 3-component NMF model was trained on the full 420-spectrum dataset to obtain discrete pseudospectral signal components and their associated contributions to each spectrum. The weighted contribution of each component in each spectrum was then plotted as a function of time to determine the relative abundance of each of the associated chemical species throughout the electrochemical cycling experiment. The spatiotemporal correlations between each of the identified component weights with one another and with the electrochemistry cycling data were calculated to assist in determination of the reaction mechanisms occurring within the electrode during cycling.

In-situ electrolyte pH measurements: *In-situ* pH measurements were collected in two-electrode cells assembled with a Zn foil anode, glass fiber separator, and cathode with a pH electrode located between the anode and cathode. A micro pH electrode (Orion 9863BN) was used where the pH of pristine 2 M $ZnSO_4$ electrolyte was measured by inserting the pH electrode immediately after cell assembly. Similarly, electrolyte pH was measured immediately after the 1st discharge and 1st charge. The pH electrode used a 10 s reporting interval.

Results

Materials and Electrochemical Characterization

Rietveld refinement of synchrotron-based X-ray diffraction of the as-synthesized material affirmed the structure to be cryptomelane-type α-MnO_2 (I4/m space group) (**Figure S1 a, Table S1**), consisting of a 2x2 MnO_6 tunneled framework with potassium atoms occupying the tunnel center. The potassium

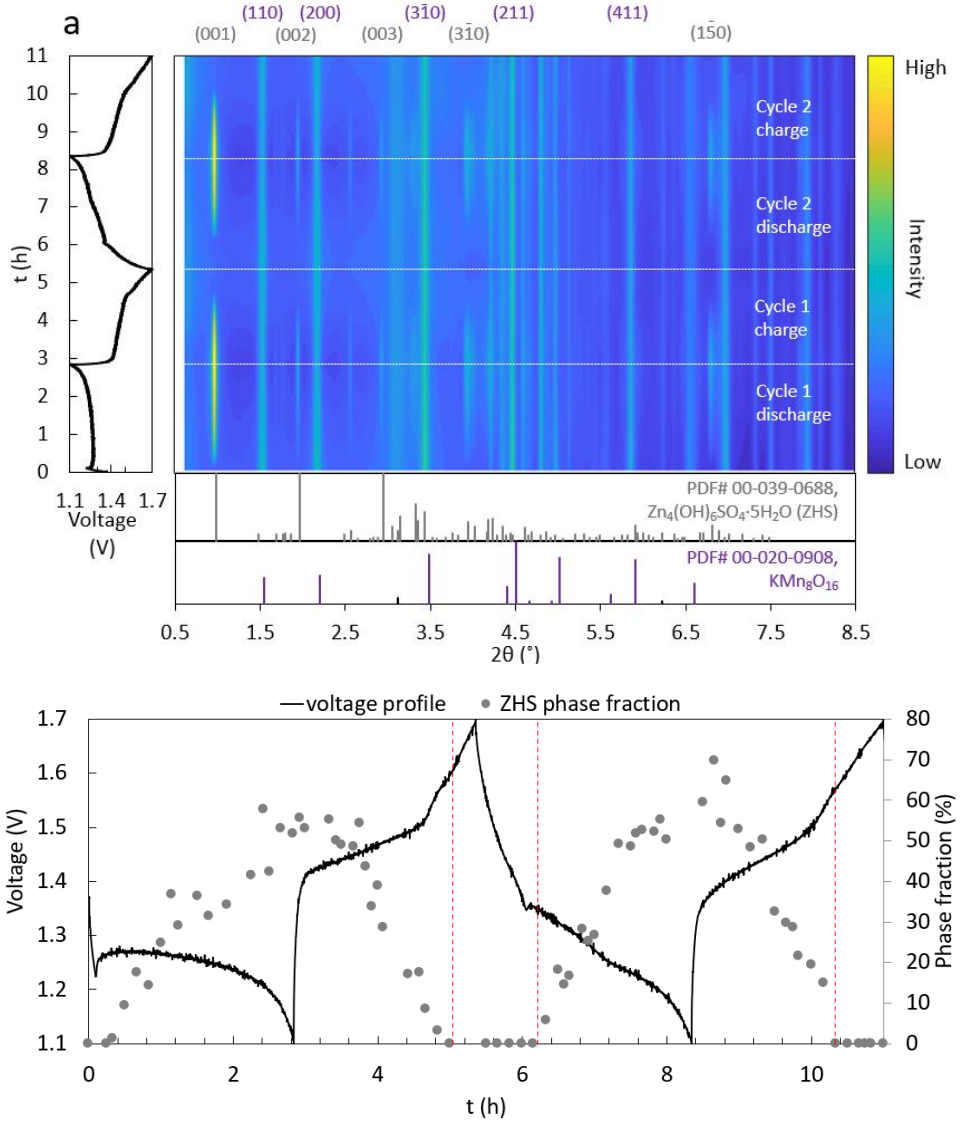

Figure 1 a Evolution of operando XRD during 1st and 2nd cycle as a function of time. **b** Voltage profile of the operando XRD cell plotted with refined ZHS phase weight fraction.

content was determined via ICP-OES, where an elemental ratio of K:Mn = 0.99:8 was measured. Water content was calculated from the TGA result (**Figure S2**) based on a previously reported method.[51] The chemical formula for the as-synthesized material is $KMn_8O_{16}{\cdot}2.31\ H_2O$ has a calculated Mn oxidation state of 3.875 based on the K/Mn ratio.

Representative galvanostatic electrochemistry of a Zn/α-MnO_2 cell are shown in **Figure S1 b**, where the potential profiles of the first two cycles are plotted versus electron equivalents per KMn_8O_{16} unit. The 1st discharge consists of one voltage plateau at ~1.2 V. The 2nd cycle discharge profile is different relative to cycle 1, where three distinct voltage plateaus are present at ~1.35 V, ~1.30 V and ~1.15 V, suggesting three different reaction stages. The 1st and 2nd cycle charge profiles are similar, consisting of two distinct voltage plateaus at ~1.50 V and ~1.65 V, which suggests two different Faradaic reaction stages.[52]

Operando X-ray Diffraction Characterization

Operando XRD was collected to probe the crystallographic changes occurring within the α-MnO_2 electrode during the 1st and 2nd cycle in the aqueous Zn/α-MnO_2 cell (**Figure 1 a, Figure S3 & S4**). The pristine pattern of the cathode is attributed to cryptomelane-type α-MnO_2 (PDF # 00-020-0908) with distinctive *a,b*-plane (1 1 0) and *c*-plane (2 0 0) peaks located at 1.5° and 2°, respectively. The peak near 3° assigned to the CNT present in the composite electrode was included as part of the background function for refinement. Peaks near 4.4° and 5° are attributed to the Zn foil anode and titanium current collectors, respectively.

During the 1st discharge, a new structure is detected with a distinguishable peak at 0.7°, which indexes to the (0 0 1) crystal plane of zinc hydroxy sulfate (ZHS, $Zn_4SO_4(OH)_6{\cdot}5H_2O$, PDF #00-060-0655) with an interplanar spacing of 10.9 Å. The occurrence of ZHS is consistent with previous reports where reversible Mn dissolution-deposition reaction dominates the electrochemistry of AZMBs.[29, 34-35, 53] The ZHS phase first appears at 0.7 electron equivalent (ee) per KMn_8O_{16} unit of discharge and as the discharge progresses, the intensity of the (0 0 1) peak increases while the α-MnO_2 (1 1 0) and (2 0 0) peaks remain visible. The *operando* XRD patterns were refined using α-MnO_2 and zinc hydroxy sulfate (ZHS, $Zn_4(OH)_6SO_4{\cdot}5H_2O$) references with additional diffraction contributions from the Zn anode and Ti current collector (**Figure S4, Tables S2-S5**). Rietveld refinements demonstrate that the phase fraction of ZHS increases from 1.2% to 53.1%; whereas, the α-MnO_2 phase fraction decreases from 91% to 42.5%, from 0.7 ee to 3.6 ee. During the 1st charge, the ZHS phase is present between 0 ee and 3.0 ee (**Figure S5**), the ZHS fraction decrease starts at 0.7 ee and drops to 0 between 3.0 ee to 3.5 ee. At the end of the 1st charge, the XRD pattern is dominated by α-MnO_2. *Operando* XRD analysis collected during 2nd discharge shows a similar two-phase crystallographic behavior between α-MnO_2 and ZHS. ZHS appears at 1.1 ee of discharge (1.32 V) and ZHS phase fraction increases with increasing depth of discharge. The ZHS phase disappears from 2.6 ee to 3.6 ee (1.5 V to 1.7 V) on 2nd charge. Notably, the lattice parameters of the α-MnO_2 and ZHS phases remain consistent throughout the 1st and 2nd cycle. The phase fraction of ZHS and α-MnO_2 were plotted with the galvanostatic cycling profile in **Figure 1 b**. A ZHS-free region is observed at the second voltage plateau during charge and continues through the first voltage plateau during the 2nd discharge. Notably, there is a smaller ZHS-free region during the 1st discharge from 0 to 0.3 ee where ZHS is not observed, which can be attributed to a Mn oxide surface protonation process prior to Mn dissolution.[54]

Ex-situ XRD Characterization

To support the findings of *operando* XRD experiment, *ex-situ* XRD was performed for cathodes cycled to different stages in pouch cells as shown in **Figure 2**. This characterization focuses on the 1st charge and 2nd discharge, which is representative for subsequent cycling. Point 1 was taken near the end of the charge stage 1, where a ZHS phase associated with the Mn dissolution reaction during the initial discharge can be identified alongside with pristine cryptomelane from the XRD pattern. As the system moves to point 2 during charge stage 2, with ZHS phase has completely vanished from the cathode, with one new broad peak visible at ~66˚ (red box in **Figure 2 b**). This peak suggests that a non-crystalline charge product has formed during this stage. The XRD pattern of the cathode remained almost unchanged until the end of charge at point 3, where the peak intensity of the charge product increased slightly, suggesting increased phase fraction. As the system moves to the 2nd discharge stage 1 at point 4, XRD pattern still resembles points 2 and 3 with only the pristine cryptomelane peak and the non-crystalline charge product visible. Peaks from ZHS can be observed at point 5 as the system moves toward discharge stage 2. Points 6 – 8 were taken from discharge stage 2 and 3, where the ZHS peak intensity gradually increased. The formation and decomposition of ZHS phases are pH-mediated as indicated from previous work,[55] which directly results from the dissolution and deposition of Mn.[35, 53] Therefore, with ZHS present during charge stage 1 and discharge stage 2 & 3, the corresponding reaction mechanism is likely Mn dissolution-deposition. Although previous works have proposed a Zn-intercalation mechanism during the discharge of AZMBs with $ZnSO_4$ electrolyte, such reaction is not likely in this work. The *ex situ* XRD results and the *operando* XRD results shown in **Figure 1** showed that no peak shift occurred to the undissolved α-MnO_2 material, indicating no structural changes, while ion intercalation to this type of material would result in significant lattice parameter changes.[56] The absence of ZHS from points 2-4 is consistent with the observation of the ZHS-free window in the *operando* XRD results above, suggesting that an alternative mechanism is dominating the system during corresponding stages.

Operando and *Ex-situ* XANES/EXAFS

Operando K-edge XANES, an element-specific technique, was used to follow changes in the Mn atomic environment, including

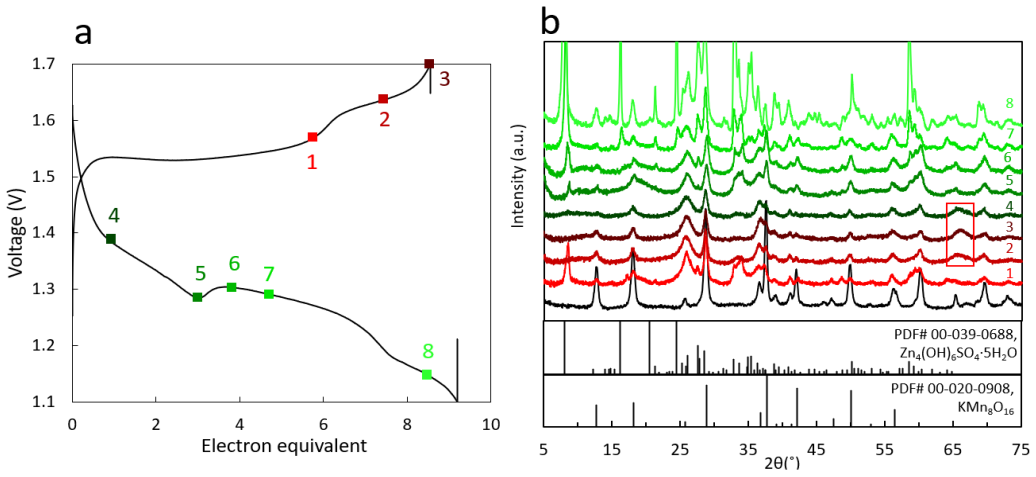

Figure 2 a Galvanostatic cycling profile for first charge and second discharge and **b** corresponding ex-situ XRD patterns of cathodes cycled to different stages as indicated.

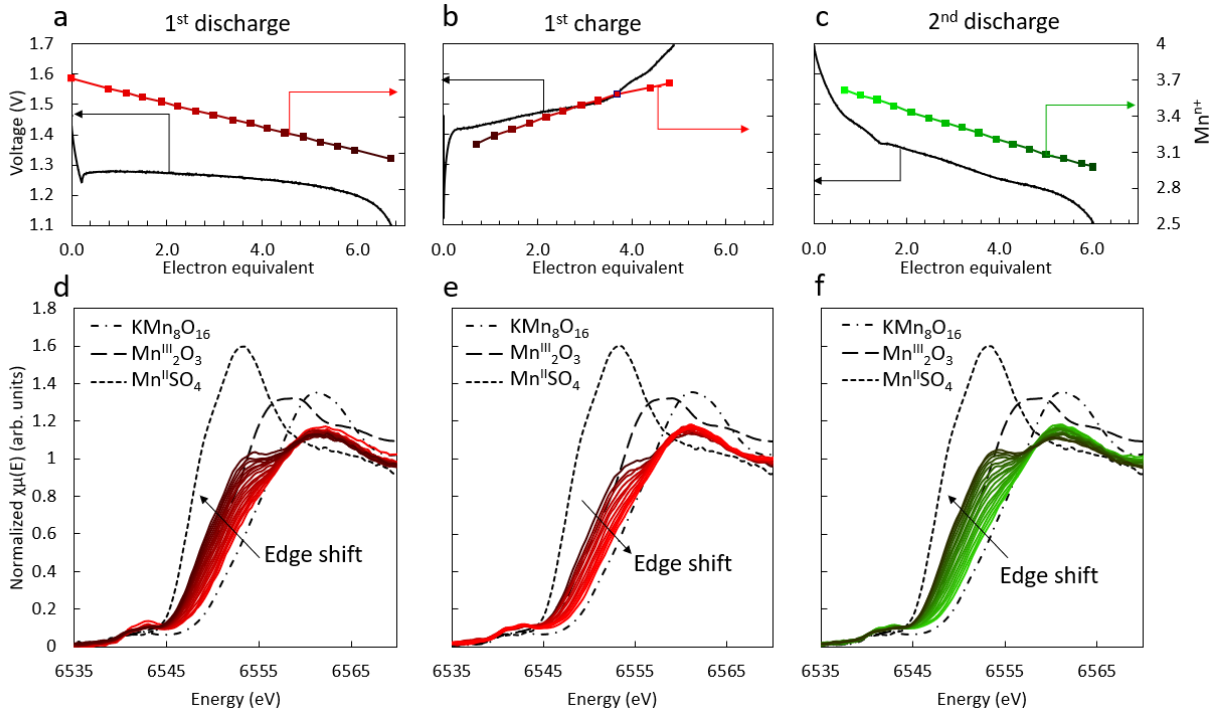

Figure 3 Galvanostatic voltage profiles plotted with average Mn oxidation states calculated with LCF fitted standard weights of the operando XANES cell during a 1st discharge, **b** 1st charge and **c** 2nd discharge with **d-f** corresponding operando XANES spectra overlays

Mn average oxidation state (AOS) (**Figure 3**). The MnO_2 standard represents Mn^{4+} in a solid lattice; whereas the dissolved $MnSO_4$ standard represents Mn^{2+} dissolved in aqueous media. Upon 1st and 2nd discharge, the absorption edge shifts to lower energy indicating a decrease of the Mn AOS (**Figure 3 a, 3 c**). The absorption edge shifts to higher energy upon charge, corresponding to an increase of the Mn AOS (**Figure 3 b**). Notably, a peak at 6550 eV increases in intensity during discharge and decreases in intensity during charge. This peak occurs at the same energy as the white line peak of the $MnSO_4$ standard, suggesting the evolution of this peak is associated with the presence of Mn^{2+} in the electrolyte. The XANES spectra collected at the pristine state and end of 1st discharge, 1st charge, and 2nd discharge are plotted (**Figure S6**). Slight differences are observed between the 1st charged and pristine spectra, indicating the Mn local atomic environment changes after charge.

Linear combination fitting (LCF) analysis using α-MnO_2 and $MnSO_4$ standards provides estimates of Mn AOS throughout the 1st and 2nd (dis)charge. An AOS of 3.875 was as sumed for the α-MnO_2 standard based on the characterized chemical formula. Results show that Mn AOS decreases linearly from $Mn^{3.875+}$ to Mn^{3+} during the 1st discharge. The measured changes in Mn AOS were used to estimate an XAS-derived specific capacity value for the 1st and 2nd (dis)charge. Notably, the XAS-derived specific capacity is similar to the specific capacity measured electrochemically (**Table 1**). There are some minor differences between the XAS-derived values and the actual values, which

Table 1. Comparison between theoretical specific capacity calculated from average Mn oxidation state change and the actual specific capacity determined from the electrochemistry.

Cycle	Mn AOS	XAS-derived specific capacity (mAh/g)	Electrochemical specific capacity (mAh/g)
1st discharge	3.1	240	248
1st charge	3.7	181	181
2nd discharge	3.0	202	223

are very likely caused by inhomogeneous Mn distribution within the *operando* cell, since XAS measurement took place inside a very small volume within the cell. The comparison in **Table 1** demonstrates that the Mn redox reaction accounts for the Faradaic capacity delivered and indicates that Mn is the primary cathodic redox-active element in the system.

Ex-situ XAS data were collected on cycled α-MnO_2 electrodes to identify the structure and composition of the charge product at the end of each potential plateau (**Figure 4 a, 4 b**). Within the radial distance of interest, the Fourier-transformed EXAFS spectra (*r*-space) of the pristine α-MnO_2 electrode yields three peaks at 1.5 Å, 2.3 Å, and 3.1 Å, corresponding to the Mn-O, Mn-Mn_{edge}, and Mn-Mn_{corner} single-scattering amplitudes.[57] Upon charge to 1.5 V and 1.7 V (end of charge), the Mn-Mn_{corner} peak intensity decreases, suggesting a collapse of the native tunnel structure. Notably, the sustained Mn-Mn_{edge} feature suggests that a 2D-planar MnO_6 octahedral arrangement is likely, consistent with the layered Zn Mn oxides observed on charge in previous reports on AZMBs,[29, 35, 53, 58] some of which report that the charge product structurally resembles the layered $ZnMn_3O_7{\cdot}3H_2O$.[35, 53] As no crystalline charge product was identified in the fully charged *operando* XRD pattern of the AZMB cathode (**Figure S4 b, d**), the actual charge product is very likely a poorly crystalline Zn Mn oxide that has a layered local structure around Mn centers. To explore the cathode local structural evolution during charge, a comparative fitting analysis was applied to the EXAFS spectra of the charged electrodes using both cryptomelane α-MnO_2 [57] and $ZnMn_3O_7{\cdot}3H_2O$ reference structures[59] generated via FEFF6, crystal structures of both reference models are shown in **Figure 4 b** and **d**.[50, 60] A two-component EXAFS fitting strategy was applied using phase fraction fitting as previously reported.[34, 61] EXAFS fitting results of the 2ee charged and fully charged cathodes are shown in **Table 2**. Note that according to literature[61], coordination number and phase fraction cannot be simultaneously fitted, therefore the coordination number of all paths were assumed to be ideal based on the structure. The fitting result indicates that a layered Mn oxide structurally resembling $ZnMn_3O_7{\cdot}3H_2O$ forms during charge stage 1, and its phase fraction increased over the charging process.

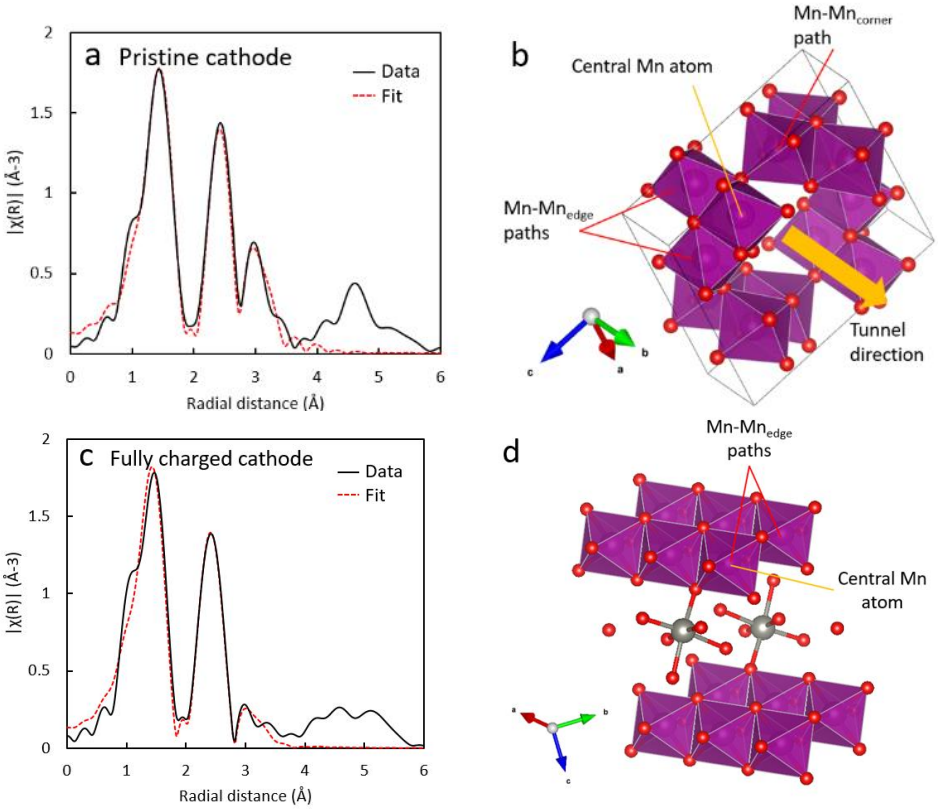

Figure 4 a EXAFS spectra of pristine KMn_8O_{16} cathode plotted with fitted result. **b** Theoretical structure of KMn_8O_{16} used for EXAFS fitting. **c** EXAFS spectra of charged KMn_8O_{16} cathode plotted with fitted result. **d** Theoretical structure of $ZnMn_3O_7{\cdot}3H_2O$ used for EXAFS fitting.

Table 2. EXAFS fitting results of the cathodes after partial charge (two electron equivalents, 2ee) and full charged (4.3 ee). Amplitude reduction factor was obtained via standard fitting to be 0.76, coordination numbers were assumed to be ideal.

Sample	Theoretical FEFF	Phase fraction	Shell	path	ΔE_0	R (Å)	σ^2	R-factor
Partially charged (2ee)	Cryptomelane (KMn_8O_{16})	0.540	1st	Mn-O	-9.29	1.86(0.04)	0.0054	0.0043
			2nd	Mn-Mn (edge)		2.78(0.02)		
				Mn-O		3.35(0.14))		
			3rd	Mn-Mn (corner)		3.40(0.03)		
	Chalcophanite ($ZnMn_3O_7 \cdot 3H_2O$)	0.460	1st	Mn-O	0.73	1.91(0.02)	0.0028	
			2nd	Mn-Mn (edge)		2.94(0.01)		
			3rd	Mn-O		3.75(0.06)		
Fully charged (4.3 ee)	Cryptomelane (KMn_8O_{16})	0.313	1st	Mn-O	4.64	1.89(0.09)	0.0030	0.017
			2nd	Mn-Mn (edge)		2.91(0.04)		
				Mn-O		3.72(0.10)		
			3rd	Mn-Mn (corner)		3.44(0.03)		
	Chalcophanite ($ZnMn_3O_7 \cdot 3H_2O$)	0.687	1st	Mn-O	-4.49	1.87(0.04)	0.0041	
			2nd	Mn-Mn (edge)		2.85(0.01)		
			3rd	Mn-O		3.52(0.07)		

Operando Raman Spectroscopy and Opto-Electrochemistry

Operando Raman spectroscopy provides insight into the structural evolution of crystalline and amorphous products during the 1st and 2nd cycle at the α-MnO_2 electrode surface (**Figure 5 a, d**). The pristine α-MnO_2 material displays three distinct Mn-O bands at 183, 579, and 639 cm^{-1}.[62] The moderately strong peak at 183 cm^{-1} is a marker for α-MnO_2 phases, which corresponds to a longer-range translational motion of the MnO_6 octahedra, arising from flexing of the octahedral framework. The position and intensity of this peak is relatively insensitive to the tunnel cation composition or fraction of octahedral Mn^{3+}.[63] During the 1st discharge (**Figure 5 b**), undissolved α-MnO_2 phase remains. At the end of the 1st charge, peaks located at 388, 507, 571, and 689 cm^{-1} are indexed to the layered Zn Mn oxide (**Figure 5 c**).[64] In the 2nd discharge (**Figure 5e**), the layered phase disappears and there are still some undissolved α-MnO_2 phases. At the end of the 2nd charge (**Figure 5 f**), the layered phase forms again.

A 3-component non-matric factorization (NMF) model successfully unmixed three interpretable signal components from the Raman dataset. Components 1, 2, and 3 are identified as ZHS/electrolyte, α-MnO_2, and layered Zn Mn oxide, respectively (**Figure S7**).[63-65] The NMF analysis reveals that the weight of layered Zn Mn oxide rises sharply during the final 2ee of each charge **Figure 5 g**). The signal intensity of the layered Zn Mn oxide component is temporally anti-correlated with that of the ZHS/electrolyte component (ρ = -0.57), revealing that the two components are mechanistically related (**Figure S7**). The layered Zn Mn oxide is visualized via optoelectrochemical testing and confirmed via *ex-situ* Raman, where at the end of charge, formation of a two-dimensional material with large lateral size forms over the graphene current collector (**Figure S8 & S9, Video S1**).

Ex-situ scanning electron microscopy of pristine and cycled electrodes

Ex-situ SEM images of the pristine and cycled electrodes were acquired to track the morphological evolution of the cathodes. The pristine α-MnO_2 material (**Figure 6a**) displayed a uniform 1D nanofiber morphology with an average diameter of 30 nm. Upon the 1st discharge, a new material emerged with submicron 2D plate-like morphology (**Figure 6b**), which can be assigned to the ZHS phase. Upon the 1st charge (**Figure 6c**), assembly of nanosheets was observed, corresponding to the layered $ZnMn_3O_7 \cdot 3H_2O$ phase, which is consistent with a previous TEM study [53] of this material observed at the charge state of a Zn/ α-MnO_2 battery. The cycle 2 discharge sample (**Figure 6d**) evinced similar morphology as the cycle 1 counterpart, consistent with the formation of ZHS phase. Interestingly, the cycle 2 charge sample (**Figure 6e**) contained a mixture of both nanoparticles and nanosheets.

In-situ pH Measurements with Derived Pourbaix Diagram

In-situ electrolyte pH measurements were conducted before electrochemical testing and after 1st discharge and charge in a two-electrode cell configuration (**Figure S10**). Before electrochemical testing, the 2 M $ZnSO_4$ electrolyte has a pH value of 4.23. At the end of the 1st discharge, the pH increases to 5.27. At the end of the 1st charge, pH slightly decreases to 5.03. Free energies were previously determined for reference solid manganese oxide materials using density function theory (DFT).[66-67] The available values were used to construct multicomponent Pourbaix Diagrams[66-67] using Pymatgen.[68-69]

Stage	Cell voltage (V)	Electrolyte pH
Pristine	1.47 (OCV)	4.23
End of 1st discharge – beginning of 1st charge	1.25	5.27
End of 1st charge – beginning of 2nd discharge	1.63	5.03

Table 3 *In-situ* cell voltage & pH measurement results at different cycling stages of the Zn/MnO_2 battery.

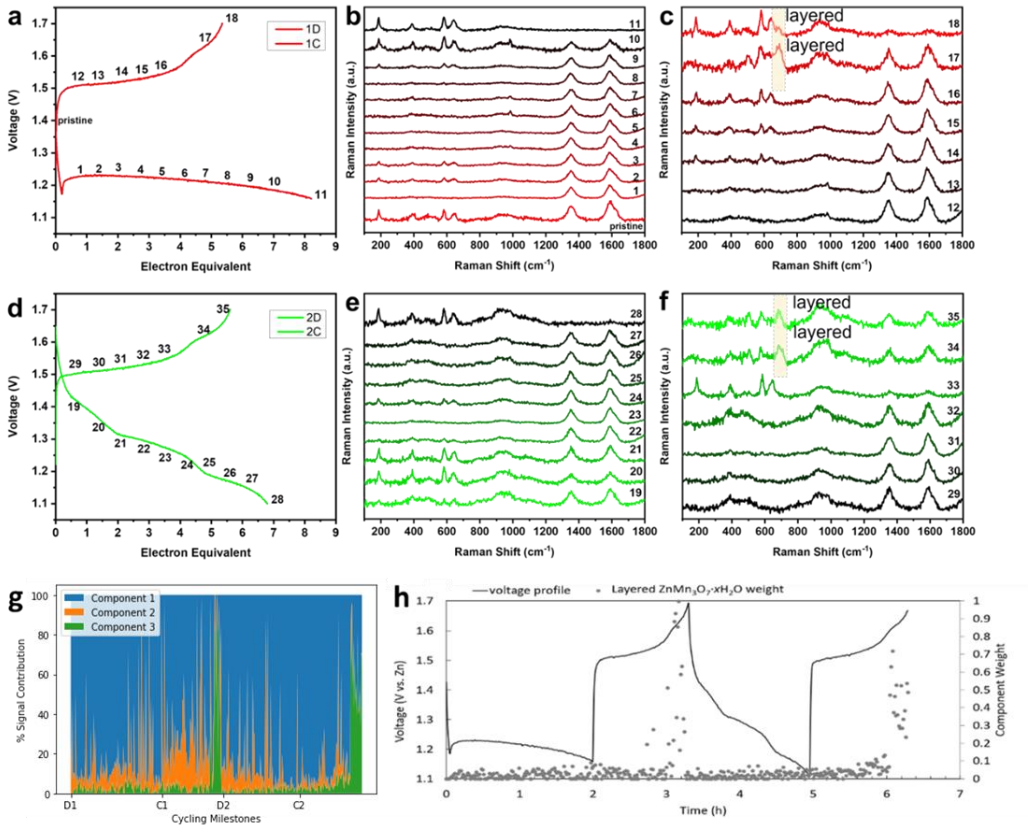

Figure 5 a Voltage profiles of the 1st cycle and selected representative operando Raman spectra acquired during **b** discharge and **c** charge (analysis of Raman data containing 420 spectra is presented in Figure S7). **d-f** Voltage profiles of the 2nd cycle and the representative Raman spectra acquired. **g** Percent signal contributions of pseudospectral components identified by non-matrix factorization (NMF) unmixing algorithm. **h** Weight fraction of layered $ZnMn_3O_7{\cdot}xH_2O$ identified via NMF with corresponding electrochemistry.

With the experimental values of electrolyte pH, Zn-Mn-O three component Pourbaix diagrams were constructed for the pristine (no Mn^{2+} present, **Figure 7 a**), fully discharged (with Mn2+ present, **Figure 7 b**) and fully charged (no Mn2+ present, **Figure 7 c**) conditions to show thermodynamically favored phase compositions within the Zn/MnO2 battery. Table 3 lists the electrolyte pH measurement results at different charge stages of the battery. The cell voltage/electrolyte pH measurement results can help locate the electrochemical environment of the AZMB at different cycling stages in the calculated Zn-Mn-O Pourbaix Diagrams, as shown in **Figure 7**. One critical factor to consider when calculating the diagram is aqueous Mn^{2+} concentration, since different Mn^{2+} concentrations will shift the thermodynamic equilibrium for the Zn/MnO_2 battery, resulting in different preferred phase regions. With such consideration in mind, cell at pristine state is represented with full red square in **Figure 7 a**, the cell at full discharged state/beginning of charge is represented by red square in **Figure 7 b** and the cell at full charged state/beginning of discharge is represented by full green square in **Figure 7 c**.

From **Figure 7 a**, we can see that Mn dissolution is expected to immediately proceed upon the 1st discharge, as the green box is located in the Zn2+ + Mn2+ phase domain and voltage decrease upon discharge will drive the cell further into the aqueous domain. However, at the end of the 1st charge/beginning of 2nd discharge as seen in **Figure 7 b**, the pH & voltage change shifts the system to Zn Mn oxide + Zn^{2+} domain as indicated by the red square. If the cell begins to charge, with the rising voltage, the system shall bypass domains (iii) and (ii), corresponding to two different Zn Mn oxide phases that are stable. This would explain the two-stage charge voltage plateau observed in Figure 7 e. As the cell moves to the end of the 1st charge/beginning of the 2nd discharge, with all Mn^{2+} redeposited and the cell voltage & electrolyte pH changes, the system can be represented by the full green box in **Figure 7 c**. Since the cell is now located in a Zn Mn oxide + Zn^{2+} domain, if the cell proceeds to the 2nd discharge, the whole system would need to bypass this solid domain before hitting the full aqueous domain again. This would explain the first discharge plateau observed over the second discharge in **Figure 7 f**. Notably, the

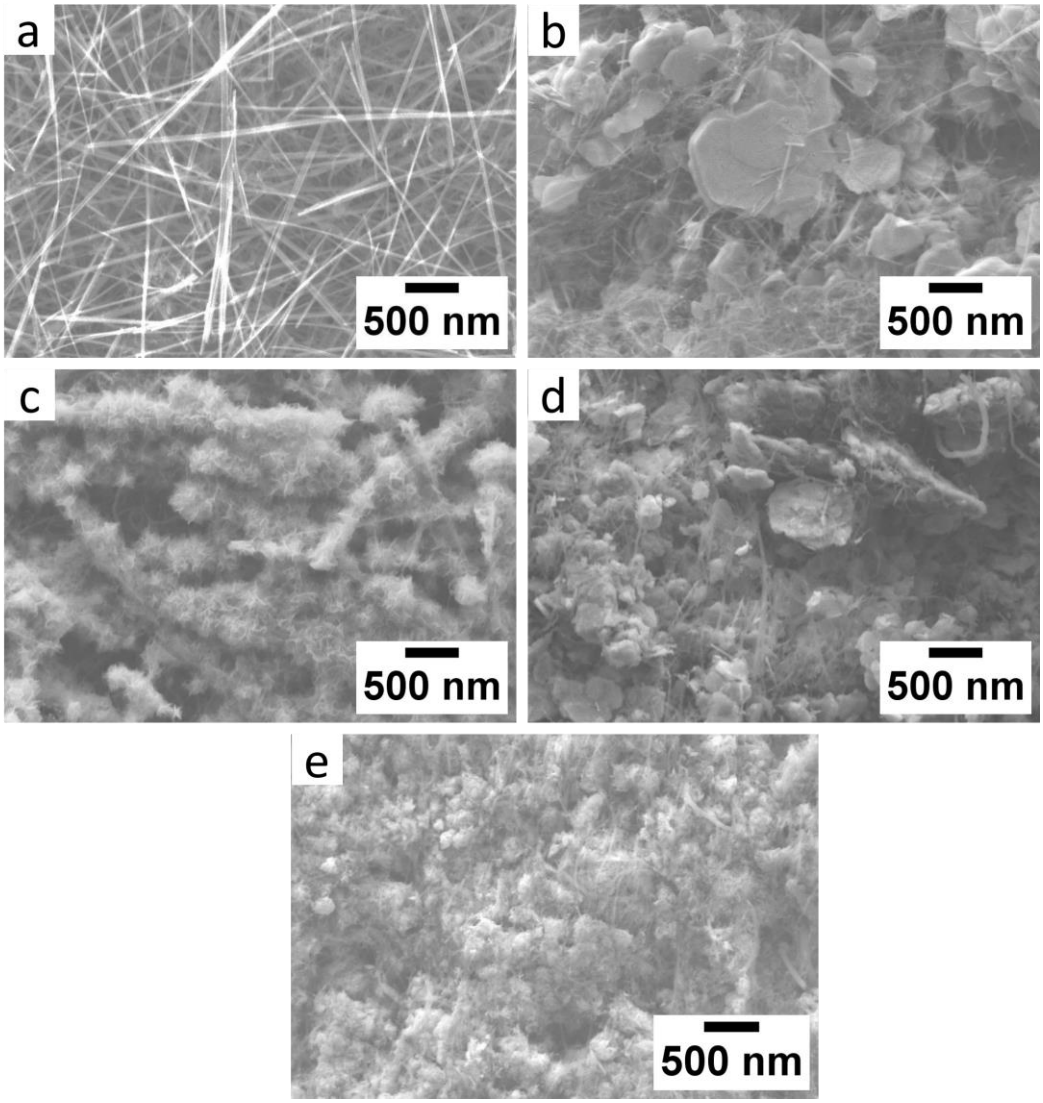

Figure 6 *Ex-situ* SEM images of electrodes at (**a**) pristine, (**b**) end of cycle 1 discharge, (**c**) end of cycle 1 charge, (**d**) end of cycle 2 discharge, and (**e**) end of cycle 2 charge states.

second and the third plateaus observed in **Figure 7 f** correspond to the dissolution of the deposited Zn Mn oxide and the pristine MnO_2, respectively. In summary, the voltage profile differences between the initial discharge and the 2nd discharge are likely the result of different electrochemical environments caused by the Mn dissolution-deposition reaction. As seen in **Figure 7 e**, the charge profiles of the AZMB over the 1st and 2nd cycle are highly similar, suggesting similar electrochemical environments. The Pourbaix Diagram calculated based on the fully discharged AZMB in **Figure 7 b** suggests that as the cell begins to charge and cell voltage rises, Mn^{2+} in the electrolyte will be deposited as Zn-Mn oxides. Based on the diagram, at least two different phases would be thermodynamically preferred depending on the cell voltage during this stage. With the continuous rise in the cell voltage, a solid phase transformation is likely to occur during charge as the system might pass two solid Zn Mn oxide phase regions during the charge process. This would explain the two plateaus observed in the charge voltage profiles.

Deriving a multi-stage dissolution-deposition mechanism

As experimental evidence and the Pourbaix diagrams in the above sections suggest, a Mn dissolution-deposition mechanism dominates the electrochemistry of the Zn/α-MnO_2 battery in this work. In the 1st discharge, we observe consistent formation of ZHS with a corresponding decrease of KMn_8O_{16} via *operando* XRD (**Figure 1**), a linear decrease in average Mn oxidation state from $Mn^{3.9+}$ to Mn^{3+} via *operando* XANES (**Figure 3**), and a single voltage plateau at ~1.25 V, indicating a Faradaic dissolution process with two coupled reactions:

$$KMn_8O_{16_{(s)}} + 32H^+ + 15e^- \rightarrow 8Mn^{2+}_{(aq)} + K^+_{(aq)} + 16H_2O \quad (1)$$

$$\frac{64}{3}Zn^{2+} + \frac{16}{3}SO_4^{2-} + 32OH^- \rightleftarrows \frac{16}{3}Zn_4(OH)_6SO_4 \quad (2)$$

$$KMn_8O_{16_{(s)}} + 16H_2O + \frac{64}{3}Zn^{2+} + \frac{16}{3}SO_4^{2-} + 15e^- \rightarrow 8Mn^{2+}_{(aq)} + K^+_{(aq)} + \frac{16}{3}Zn_4(OH)_6SO_4 \quad (3)$$

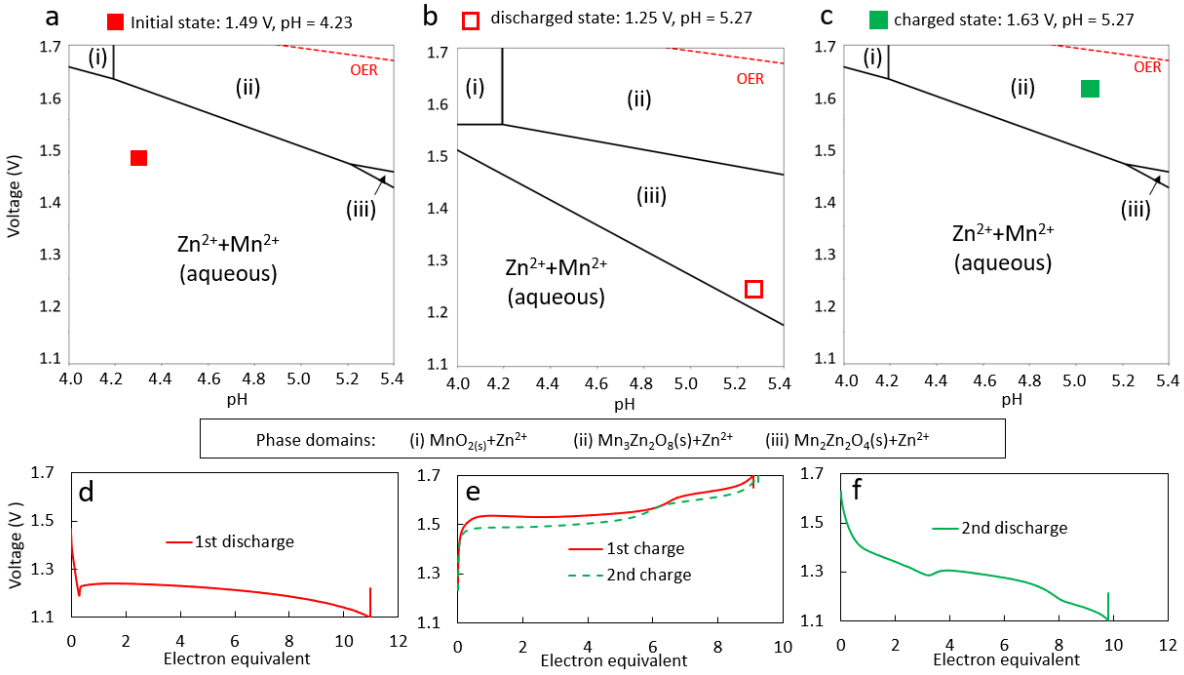

Figure 7 Pourbaix diagrams of Zn-Mn-O with the experimental pH and potential window shown with voltage of the cell electrochemistry at **a,d** Pristine state, with only Zn^{2+} present; **b,e** Fully discharged state, where a Mn^{2+} concentration of 0.2 M was used for the calculations and **c,f** fully charged state with only Zn^{2+} present.

In **reaction 1**, KMn_8O_{16} dissolves upon initial reduction to form Mn^{2+} and OH^- ions. The release of OH^- increases local electrolyte pH and promotes precipitation of ZHS in **reaction 2**,[55] the pH increase as verified by the *in-situ* measurement results presented in **Table 3**. On 1st charge, the ZHS disappears and the Mn AOS increases. Assuming **reactions 1** and **2** are reversible and the only redox mechanism, dissolution of the ZHS phase should proceed throughout the entire charge step. However, we observe a ZHS-free region from 1.5 V to 1.7 V via *operando* XRD (**Figure 1 b**). The presence of a ZHS-free region and observation of two voltage plateaus suggests that the charge mechanism is not a single-stage process.

Operando Raman spectroscopy, *operando* optoelectrochemical, and *ex-situ* EXAFS measurements all indicate the formation of a layered Zn Mn oxide on 1st charge by 1.5 V vs. Zn. This layered phase disappears during the 2nd discharge, suggesting this structure is an electrochemically formed and an electrochemically reversible product within the Zn/MnO_2 cell. Moreover, the NMF analysis of the Raman data reveals an anticorrelation between ZHS and layered Zn Mn oxide during cycling, suggesting that the layered Zn Mn oxide is related to ZHS, as shown in the proposed charge **reaction 4**.

$$8Mn^{2+} + \frac{16}{3}Zn_4(OH)_6SO_4 - je^- \rightleftarrows 8Zn_xMn^{y+}O_2 + (\frac{64}{3} - 8x)Zn^{2+} + \frac{16}{3}SO_4^{2-} + 16H_2O \quad (4)$$

This reaction represents charge stage 1 before the cell enters the ZHS-free region, as all the ZHS precipitated during initial discharge are dissolved. This reaction stage, corresponding to Mn deposition, accounts for ~80% of the cell capacity, as observed in the electrochemistry demonstrated in this work (**Figure 1 b**, **Figure 2 a**, **Figure 3 b**, **Figure 5 d**, **Figure 7 e**). As indicated by the cell electrochemistry, although all the dissolved Mn^{2+} has been precipitated as a Zn-Mn-O compound, the electron equivalents transferred at the end of charge stage 1 are less than the initial discharge ($j < 15$), thus the Mn AOS in the charge product should be lower than pristine ($y < 3.875$). This is supported by the *operando* XANES results in **Figure 3**. As a result, all the ZHS precipitated during the discharge will be fully consumed before the end of charge, which leads to charge stage 2. ZHS is a pH-sensitive compound that will be stabilized in aqueous $ZnSO_4$ electrolytes with a pH value that is slightly above 5, where further increases in pH will directly result in ZHS precipitation and any decrease in pH will result in ZHS dissolution.[55] In other words, ZHS effectively buffers the pH of the AZMB battery electrolyte during cycling. In its absence during charge stage 2, any redox activity involving aqueous ions would be unbuffered, however, electrolyte pH upon full charge was still stabilized at ~5 as shown in **Table 3**. This suggests that charge stage 2 is likely a redox reaction involving only the solid Zn-Mn compounds.

A recent study on Zn/MnO_2 battery using an electrochemical quartz crystal microbalance (EQCM) provided experimental signs of a Zn extraction reaction during the final charging stage of AZMB.[26] Layered Zn Mn oxide was also reported to be able to host excess Zn^{2+} ions and serve as a site for a Zn^{2+} extraction reaction.[70] Capability for layered Mn oxide to exhibit high-capacity, battery-like Zn^{2+} insertion and pseudocapacitive charge storage in near neutral pH electrolyte was recently demonstrated.[71] Therefore, it is likely here that a Zn-rich layered Zn Mn oxide forms as the Mn deposition product during charge stage 1, with the Mn in the compound being further oxidized during charge stage 2, Zn extraction reaction shall occur:

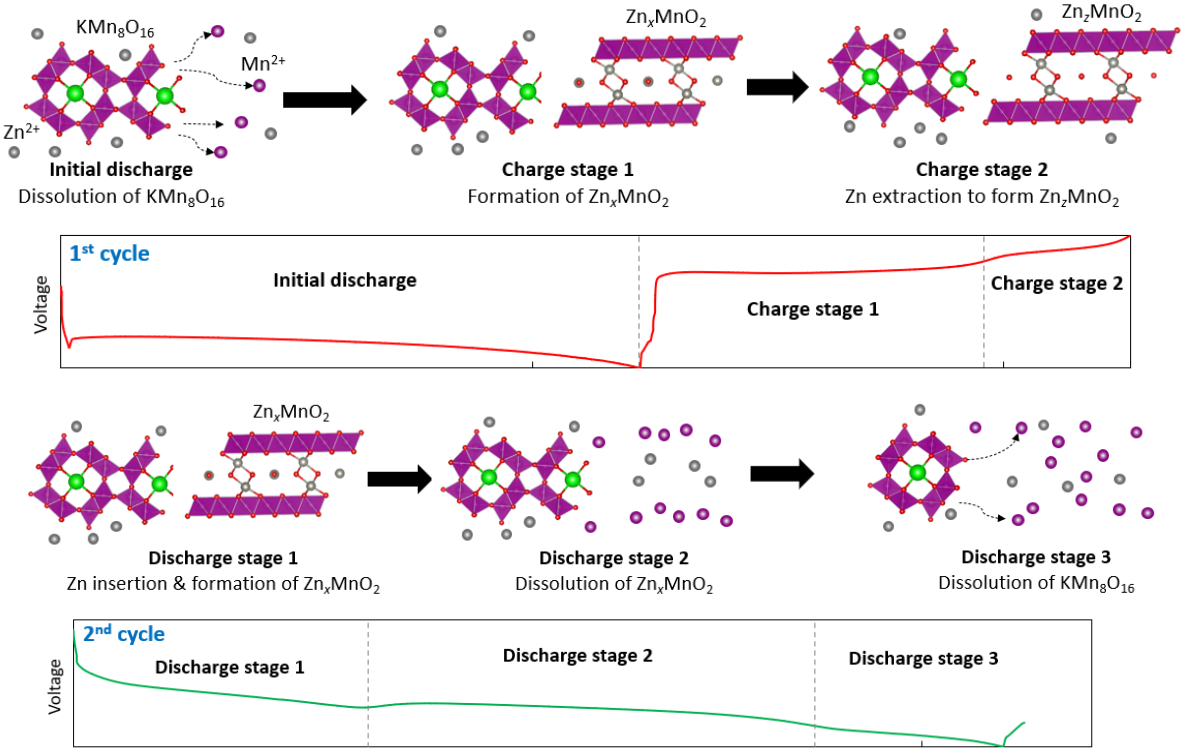

Figure 8 Conceptual schematic of the reaction mechanisms during cycle 1 and cycle 2 in the Zn/α-MnO_2 cell with 2 M $ZnSO_4$ electrolyte.

$$8Zn_xMnO_2 - ke^- \rightleftarrows 8Zn_zMnO_2 + 8(x-z)Zn^{2+}_{aq} \quad (5)$$

Where k is the electron equivalent transferred during charge stage 2 and z is the final Zn content of the layered Zn Mn oxide. Notably, j and k should vary based on the electrode and electrolyte conditions for a given system at a given stage, the Zn content z shall correspondingly vary. For example, consider a fully reversible Mn dissolution-deposition mechanism, $j + k = 15$, Zn content would then be z = 0.0625. Based on the Pourbaix Diagrams calculated under mildly acidic environments with Zn^{2+} and Mn^{2+} species in **Figure 7**, Zn-Mn-O compounds are the stable solid-state phases upon charge for AZMBs. Given that the ZHS-free region encompasses both charge stage 2 and discharge stage 1, it is reasonable to assume that **reaction 5** is reversible, therefore Zn insertion reaction is likely the main reaction during discharge stage 1.

Figure 8 summarizes the reaction mechanisms proposed during cycle 1 and cycle 2 in the Zn/α-MnO_2 cell with 2 M $ZnSO_4$ electrolyte. The 1st discharge proceeds with Mn^{2+} generation, the formation of ZHS due to an increase in electrolyte pH. During charge stage 1, Zn-Mn co-precipitation coupled with ZHS decomposition occurs. This stage, which also depletes Mn^{2+} in the electrolyte from the initial dissolution, results in a Zn-rich Zn Mn oxide with a similar crystal structure to layered $ZnMn_3O_7{\cdot}xH_2O$. In charge stage 2, Zn^{2+} is extracted from the Zn-rich Zn Mn oxide. During this stage, the layered structure is retained and Mn within the layered structure continues to oxidize. During the 2nd discharge stage 1, Zn^{2+} inserts into the structure layered structure with no dissolut ion, consistent with the observed ZHS-free region. During 2nd discharge stage 2, Mn^{2+} dissolves from the layered Zn Mn oxide charge product and ZHS precipitation occurs. The 2nd discharge stage 3 is only present when dissolution of the residual pristine α-MnO_2 continues.[35, 53] The 2nd charge demonstrates the same reaction progress as the 1st charge.

Conclusions

In this work, several complimentary *operando* techniques were utilized to characterize the reaction mechanism of a rechargeable aqueous Zn/α-MnO_2 battery with mildly acidic electrolyte. O*perando* XRD was used to characterize the evolution of ZHS, demonstrating that ZHS is closely coupled with the Mn dissolution-deposition reaction. *Operando* & *ex-situ* XAS as well as Raman spectroscopy experiments revealed the formation of a layered Zn Mn oxide phase in the cathode upon the 1st charge, demonstrating that the layered phase is the bulk-level reversible redox-active component of the aqueous Zn/α-MnO_2 system. NMF analysis of the Raman spectroscopy data and quantitative analysis of *operando* XRD data showed that the formation and dissolution of ZHS is closely correlated to the reversible electrochemical reactions of the Zn/α-MnO_2 battery. Additionally, support of the proposed mechanism uses Pourbaix Diagrams with corresponding experimental pH measurements.

A comprehensive reaction multi-stage mechanism for a rechargeable aqueous Zn/α-MnO_2 battery with $ZnSO_4$ electrolyte is proposed based on the above analysis. Identification of the reversible active material and detailed assignment of the different reactions during cycle 1 and cycle 2 are shown that provide important insight toward understanding and controlling Zn/MnO_2 electrochemical function. These results demonstrate the reversibility of the ZHS-assisted Mn deposition reaction with the cyclic formation/decomposition of the reaction by-product ZHS. As ZHS-assisted Mn dissolution-

deposition accounts for the majority of electrochemical capacity of the battery, future research efforts can be invested into promoting the ZHS-assisted Mn dissolution-deposition while suppressing side reactions.

Conflicts of interest

There are no conflicts to declare.

Acknowledgements

This work was supported as part of the Center for Mesoscale Transport Properties, an Energy Frontier Research Center supported by the U.S. Department of Energy, Office of Science, Basic Energy Sciences via grant #DE-SC0012673. The synchrotron measurements were conducted at the X-ray Powder Diffraction (XPD, 28-ID-2) the Quick X-ray Absorption and Scattering (QAS, 7-BM) of the National Synchrotron Light Source II (NSLS-II) which is a U.S. DOE Office of Science Facility, at Brookhaven National Laboratory under Contract No. DE-SC0012704. Brookhaven National Laboratory is acknowledged for support of the cell development associated with the *operando* x-ray diffraction measurement. EST acknowledges support from the William and Jane Knapp Chair in Energy and the Environment.

Notes and references

1. Dunn, B.; Kamath, H.; Tarascon, J.-M., Electrical Energy Storage for the Grid: A Battery of Choices. **2011,** *334* (6058), 928-935.

2. Soloveichik, G. L., Battery Technologies for Large-Scale Stationary Energy Storage. *Annual Review of Chemical and Biomolecular Engineering* **2011,** *2* (1), 503-527.

3. Zhu, Z.; Jiang, T.; Ali, M.; Meng, Y.; Jin, Y.; Cui, Y.; Chen, W., Rechargeable Batteries for Grid Scale Energy Storage. *Chemical Reviews* **2022,** *122* (22), 16610–16751.

4. Gao, X.; Wu, H.; Li, W.; Tian, Y.; Zhang, Y.; Wu, H.; Yang, L.; Zou, G.; Hou, H.; Ji, X., H+-Insertion Boosted α-MnO2 for an Aqueous Zn-Ion Battery. *Small* **2020,** *n/a* (n/a), 1905842.

5. Liu, Z. X.; Huang, Y.; Huang, Y.; Yang, Q.; Li, X. L.; Huang, Z. D.; Zhi, C. Y., Voltage issue of aqueous rechargeable metal-ion batteries. *Chemical Society Reviews* **2020,** *49* (1), 180-232.

6. Jia, X.; Liu, C.; Neale, Z. G.; Yang, J.; Cao, G., Active Materials for Aqueous Zinc Ion Batteries: Synthesis, Crystal Structure, Morphology, and Electrochemistry. *Chem. Rev. (Washington, DC, U. S.)* **2020,** *120* (15), 7795-7866.

7. Konarov, A.; Voronina, N.; Jo, J. H.; Bakenov, Z.; Sun, Y.-K.; Myung, S.-T., Present and Future Perspective on Electrode Materials for Rechargeable Zinc-Ion Batteries. *ACS Energy Letters* **2018,** *3* (10), 2620-2640.

8. Ghosh, S. K., Diversity in the Family of Manganese Oxides at the Nanoscale: From Fundamentals to Applications. *ACS Omega* **2020,** *5* (40), 25493-25504.

9. Ching, S.; Suib, S. L., Synthetic Routes to Microporous Manganese Oxides. *Comments on Inorganic Chemistry* **1997,** *19* (5), 263-282.

10. Pan, H.; Shao, Y.; Yan, P.; Cheng, Y.; Han, K. S.; Nie, Z.; Wang, C.; Yang, J.; Li, X.; Bhattacharya, P.; Mueller, K. T.; Liu, J., Reversible aqueous zinc/manganese oxide energy storage from conversion reactions. *Nature Energy* **2016,** *1* (5), 16039.

11. Chamoun, M.; Brant, W. R.; Tai, C.-W.; Karlsson, G.; Noréus, D., Rechargeability of aqueous sulfate Zn/MnO2 batteries enhanced by accessible Mn2+ ions. *Energy Storage Materials* **2018,** *15*, 351-360.

12. Lee, B.; Yoon, C. S.; Lee, H. R.; Chung, K. Y.; Cho, B. W.; Oh, S. H., Electrochemically-induced reversible transition from the tunneled to layered polymorphs of manganese dioxide. *Scientific Reports* **2014,** *4* (1), 6066.

13. Alfaruqi, M. H.; Gim, J.; Kim, S.; Song, J.; Pham, D. T.; Jo, J.; Xiu, Z.; Mathew, V.; Kim, J., A layered δ-MnO2 nanoflake cathode with high zinc-storage capacities for eco-friendly battery applications. *Electrochemistry Communications* **2015,** *60*, 121-125.

14. Xu, D.; Li, B.; Wei, C.; He, Y.-B.; Du, H.; Chu, X.; Qin, X.; Yang, Q.-H.; Kang, F., Preparation and characterization of MnO2/acid-treated CNT nanocomposites for energy storage with zinc ions. *Electrochimica Acta* **2014,** *133*, 254-261.

15. Xu, C.; Li, B.; Du, H.; Kang, F., Energetic Zinc Ion Chemistry: The Rechargeable Zinc Ion Battery. *Angewandte Chemie International Edition* **2012,** *51* (4), 933-935.

16. Lee, B.; Lee, H. R.; Kim, H.; Chung, K. Y.; Cho, B. W.; Oh, S. H., Elucidating the intercalation mechanism of zinc ions into α-MnO2 for rechargeable zinc batteries. *Chemical Communications* **2015,** *51* (45), 9265-9268.

17. Sun, W.; Wang, F.; Hou, S.; Yang, C.; Fan, X.; Ma, Z.; Gao, T.; Han, F.; Hu, R.; Zhu, M.; Wang, C., Zn/MnO2 Battery Chemistry With H+ and Zn2+ Coinsertion. *Journal of the American Chemical Society* **2017,** *139* (29), 9775-9778.

18. Zhang, N.; Cheng, F.; Liu, J.; Wang, L.; Long, X.; Liu, X.; Li, F.; Chen, J., Rechargeable aqueous zinc-manganese dioxide batteries with high energy and power densities. *Nature Communications* **2017,** *8* (1), 405.

19. Zheng, J.; Zhao, Q.; Liu, X.; Tang, T.; Bock, D. C.; Bruck, A. M.; Tallman, K. R.; Housel, L. M.; Kiss, A. M.; Marschilok, A. C.; Takeuchi, E. S.; Takeuchi, K. J.; Archer, L. A., Nonplanar Electrode Architectures for Ultrahigh Areal Capacity Batteries. *ACS Energy Letters* **2018**, 271-275.

20. Huang, Y.; Mou, J.; Liu, W.; Wang, X.; Dong, L.; Kang, F.; Xu, C., Novel Insights into Energy Storage Mechanism of Aqueous Rechargeable Zn/MnO2 Batteries with Participation of Mn2+. *Nano-Micro Letters* **2019,** *11* (1), 49.

21. Pan, H.; Shao, Y.; Yan, P.; Cheng, Y.; Han, K. S.; Nie, Z.; Wang, C.; Yang, J.; Li, X.; Bhattacharya, P.; Mueller, K. T.; Liu, J., Reversible aqueous zinc/manganese oxide energy storage from conversion reactions. *Nature Energy* **2016,** *1*, 16039.

22. Xu, C.; Du, H.; Li, B.; Kang, F.; Zeng, Y., Reversible Insertion Properties of Zinc Ion into Manganese Dioxide and Its Application for Energy Storage. *Electrochemical and Solid-State Letters* **2009,** *12* (4), A61-A65.

23. Fitz, O.; Bischoff, C.; Bauer, M.; Gentischer, H.; Birke, K. P.; Henning, H. M.; Biro, D., Electrolyte Study with in Operando pH Tracking Providing Insight into the Reaction Mechanism of Aqueous Acidic Zn//MnO2 Batteries. *Chemelectrochem* **2021,** *8* (18), 3553-3566.

24. Guo, X.; Zhou, J.; Bai, C.; Li, X.; Fang, G.; Liang, S., Zn/MnO2 battery chemistry with dissolution-deposition mechanism. *Materials Today Energy* **2020,** *16*, 100396.

25. Moon, H.; Ha, K.-H.; Park, Y.; Lee, J.; Kwon, M.-S.; Lim, J.; Lee, M.-H.; Kim, D.-H.; Choi, J. H.; Choi, J.-H.; Lee, K. T., Direct Proof of the Reversible Dissolution/Deposition of Mn2+/Mn4+ for Mild-Acid Zn-MnO2 Batteries with Porous Carbon Interlayers. *Advanced Science* **2021,** *8* (6), 2003714.

26. Rodríguez-Pérez, I. A.; Chang, H. J.; Fayette, M.; Sivakumar, B. M.; Choi, D.; Li, X.; Reed, D., Mechanistic investigation of redox processes in Zn–MnO2 battery in mild aqueous electrolytes. *Journal of Materials Chemistry A* **2021,** *9* (36), 20766-20775.

27. Shen, X.; Wang, X.; Zhou, Y.; Shi, Y.; Zhao, L.; Jin, H.; Di, J.; Li, Q., Highly Reversible Aqueous Zn-MnO2 Battery by Supplementing Mn2+-Mediated MnO2 Deposition and Dissolution. *Advanced Functional Materials* **2021,** *31* (27), 2101579.

28. Liang, G.; Mo, F.; Li, H.; Tang, Z.; Liu, Z.; Wang, D.; Yang, Q.; Ma, L.; Zhi, C., A Universal Principle to Design Reversible Aqueous Batteries Based on Deposition–Dissolution Mechanism. **2019,** *9* (32), 1901838.

29. Kim, S. J.; Wu, D.; Housel, L. M.; Wu, L.; Takeuchi, K. J.; Marschilok, A. C.; Takeuchi, E. S.; Zhu, Y., Toward the Understanding of the Reaction Mechanism of Zn/MnO2 Batteries Using Non-alkaline Aqueous Electrolytes. *Chemistry of Materials* **2021,** *33* (18), 7283-7289.

30. Wu, D. R.; Housel, L. M.; Kim, S. J.; Sadique, N.; Quilty, C. D.; Wu, L. J.; Tappero, R.; Nicholas, S. L.; Ehrlich, S.; Zhu, Y. M.; Marschilok, A. C.; Takeuchi, E. S.; Bock, D. C.; Takeuchi, K. J., Quantitative temporally and spatially resolved X-ray fluorescence microprobe characterization of the manganese dissolution-deposition mechanism in aqueous Zn/alpha-MnO2 batteries. *Energy & Environmental Science* **2020,** *13* (11), 4322-4333.

31. Kim, S. J.; Wu, D. R.; Sadique, N.; Quilty, C. D.; Wu, L. J.; Marschilok, A. C.; Takeuchi, K. J.; Takeuchi, E. S.; Zhu, Y. M., Unraveling the Dissolution-Mediated Reaction Mechanism of alpha-MnO2 Cathodes for Aqueous Zn-Ion Batteries. *Small* **2020,** *16* (48).

32. Fitz, O.; Bischoff, C.; Bauer, M.; Gentischer, H.; Birke, K. P.; Henning, H.-M.; Biro, D., Electrolyte Study with in Operando pH Tracking Providing Insight into the Reaction Mechanism of Aqueous Acidic Zn//MnO2 Batteries. *ChemElectroChem* **2021,** *8* (18), 3553-3566.

33. Bischoff, C. F.; Fitz, O. S.; Burns, J.; Bauer, M.; Gentischer, H.; Birke, K. P.; Henning, H.-M.; Biro, D., Revealing the Local pH Value Changes of Acidic Aqueous Zinc Ion Batteries with a Manganese Dioxide Electrode during Cycling. *Journal of The Electrochemical Society* **2020,** *167* (2), 020545.

34. Wu, D.; Housel, L. M.; King, S. T.; Mansley, Z. R.; Sadique, N.; Zhu, Y.; Ma, L.; Ehrlich, S. N.; Zhong, H.; Takeuchi, E. S.; Marschilok, A. C.; Bock, D. C.; Wang, L.; Takeuchi, K. J., Simultaneous Elucidation of Solid and Solution Manganese Environments via Multiphase Operando Extended X-ray Absorption Fine Structure Spectroscopy in Aqueous Zn/MnO2 Batteries. *Journal of the American Chemical Society* **2022,** *144* (51), 23405-23420.

35. Kim, S. J.; Wu, D.; Sadique, N.; Quilty, C. D.; Wu, L.; Marschilok, A. C.; Takeuchi, K. J.; Takeuchi, E. S.; Zhu, Y., Unraveling the Dissolution-Mediated Reaction Mechanism of α-MnO2 Cathodes for Aqueous Zn-Ion Batteries. **2020,** *16* (48), 2005406.

36. Wu, Y.; Zhi, J.; Han, M.; Liu, Z.; Shi, Q.; Liu, Y.; Chen, P., Regulating proton distribution by ion exchange resin to achieve long lifespan aqueous Zn-MnO2 battery. *Energy Storage Materials* **2022,** *51*, 599-609.

37. Liu, Z.; Yang, Y.; Lu, B.; Liang, S.; Fan, H. J.; Zhou, J., Insights into complexing effects in acetate-based Zn-MnO2 batteries and performance enhancement by all-round strategies. *Energy Storage Materials* **2022,** *52*, 104-110.

38. Liu, Z.; Yang, Y.; Liang, S.; Lu, B.; Zhou, J., pH-Buffer Contained Electrolyte for Self-Adjusted Cathode-Free Zn–MnO2 Batteries with Coexistence of Dual Mechanisms. *Small Structures* **2021,** *2* (11), 2100119.

39. Zeng, X.; Liu, J.; Mao, J.; Hao, J.; Wang, Z.; Zhou, S.; Ling, C. D.; Guo, Z., Toward a Reversible Mn4+/Mn2+ Redox Reaction and Dendrite-Free Zn Anode in Near-Neutral Aqueous Zn/MnO2 Batteries via Salt Anion Chemistry. **2020,** *10* (32), 1904163.

40. Liang, G.; Mo, F.; Li, H.; Tang, Z.; Liu, Z.; Wang, D.; Yang, Q.; Ma, L.; Zhi, C., A Universal Principle to Design Reversible Aqueous Batteries Based on Deposition–Dissolution Mechanism. *Advanced Energy Materials* **2019,** *9* (32), 1901838.

41. Chen, X.; Li, W.; Zeng, Z.; Reed, D.; Li, X.; Liu, X., Engineering stable Zn-MnO2 batteries by synergistic stabilization between the carbon nanofiber core and birnessite-MnO2 nanosheets shell. *Chemical Engineering Journal* **2021,** *405*, 126969.

42. Liu, W.; Zhang, X.; Huang, Y.; Jiang, B.; Chang, Z.; Xu, C.; Kang, F., β-MnO2 with proton conversion mechanism in rechargeable zinc ion battery. *Journal of Energy Chemistry* **2021,** *56*, 365-373.

43. Wu, T.-H.; Lin, Y.-Q.; Althouse, Z. D.; Liu, N., Dissolution–Redeposition Mechanism of the MnO2 Cathode in Aqueous Zinc-Ion Batteries. *ACS Applied Energy Materials* **2021,** *4* (11), 12267-12274.

44. Chao D, Z. W. Y. C. Z. Q. C. Y. G. L. D. K.; Qiao, S. Z., An electrolytic Zn-MnO2 battery for high-voltage and scalable energy storage. *Angew. Chem., Int. Ed. Engl.* **2019,** *58*, 7823.

45. Xie, C.; Li, T.; Deng, C.; Song, Y.; Zhang, H.; Li, X., A highly reversible neutral zinc/manganese battery for stationary energy storage. *Energy & Environmental Science* **2020,** *13* (1), 135-143.

46. Li, G.; Chen, W.; Zhang, H.; Gong, Y.; Shi, F.; Wang, J.; Zhang, R.; Chen, G.; Jin, Y.; Wu, T.; Tang, Z.; Cui, Y., Membrane-Free Zn/MnO2 Flow Battery for Large-Scale Energy Storage. **2020,** *10* (9), 1902085.

47. Chen, W.; Li, G.; Pei, A.; Li, Y.; Liao, L.; Wang, H.; Wan, J.; Liang, Z.; Chen, G.; Zhang, H.; Wang, J.; Cui, Y., A manganese–hydrogen battery with potential for grid-scale energy storage. *Nature Energy* **2018,** *3* (5), 428-435.

48. Yuan, J.; Liu, X.; Akbulut, O.; Hu, J.; Suib, S. L.; Kong, J.; Stellacci, F., Superwetting nanowire membranes for selective absorption. *Nature Nanotechnology* **2008,** *3* (6), 332-336.

49. Toby, B.; Dreele, R., GSAS-II: The Genesis of a Modern Open-Source All-Purpose Crystallography Software Package. *Journal of Applied Crystallography* **2013,** *46*, 544-549.

50. Ravel, B.; Newville, M., ATHENA, ARTEMIS, HEPHAESTUS: data analysis for x-ray absorption spectroscopy using IFEFFIT. *J. Synchrotron Radiat.* **2005,** *12* (4), 537-541.

51. Chen, J.; Tang, X.; Liu, J.; Zhan, E.; Li, J.; Huang, X.; Shen, W., Synthesis and Characterization of Ag−Hollandite Nanofibers and Its Catalytic Application in Ethanol Oxidation. *Chemistry of Materials* **2007,** *19* (17), 4292-4299.

52. Bard, A. J.; Faulkner, L. R.; Leddy, J.; Zoski, C. G., *Electrochemical methods: fundamentals and applications*. wiley New York: **1980**; Vol. 2.

53. Wu, D.; Housel, L. M.; Kim, S. J.; Sadique, N.; Quilty, C. D.; Wu, L.; Tappero, R.; Nicholas, S. L.; Ehrlich, S.; Zhu, Y.; Marschilok, A. C.; Takeuchi, E. S.; Bock, D. C.; Takeuchi, K. J., Quantitative temporally and spatially resolved X-ray fluorescence microprobe characterization of the manganese dissolution-deposition mechanism in aqueous Zn/α-MnO2 batteries. *Energy & Environmental Science* **2020,** *13* (11), 4322-4333.

54. Artamonova, I.; Gorichev, I.; Godunov, E., Kinetics of manganese oxides dissolution in sulphuric acid solutions containing oxalic acid. *Engineering* **2013,** *5* (9), 714-719.

55. Lee, B.; Seo, H. R.; Lee, H. R.; Yoon, C. S.; Kim, J. H.; Chung, K. Y.; Cho, B. W.; Oh, S. H., Critical Role of pH Evolution of Electrolyte in the Reaction Mechanism for Rechargeable Zinc Batteries. *ChemSusChem* **2016,** *9* (20), 2948-2956.

56. Xu, F.; Wu, L.; Meng, Q.; Kaltak, M.; Huang, J.; Durham, J. L.; Fernandez-Serra, M.; Sun, L.; Marschilok, A. C.; Takeuchi, E. S.; Takeuchi, K. J.; Hybertsen, M. S.; Zhu, Y., Visualization of lithium-ion transport and phase evolution within and between manganese oxide nanorods. *Nature Communications* **2017,** *8* (1), 15400.

57. Vicat, J.; Fanchon, E.; Strobel, P.; Tran Qui, D., The structure of K1.33Mn8O16 and cation ordering in hollandite-type structures. **1986,** *42* (2), 162-167.

58. Zhao, S.; Han, B.; Zhang, D.; Huang, Q.; Xiao, L.; Chen, L.; Ivey, D. G.; Deng, Y.; Wei, W., Unravelling the reaction chemistry and degradation mechanism in aqueous Zn/MnO2 rechargeable batteries. *Journal of Materials Chemistry A* **2018,** *6* (14), 5733-5739.

59. Wadsley, A., The crystal structure of chalcophanite, ZnMn3O7.3H2O. *Acta Crystallographica* **1955,** *8* (3), 165-172.

60. Mustre de Leon, J.; Rehr, J. J.; Zabinsky, S. I.; Albers, R. C., Ab initio curved-wave x-ray-absorption fine structure. *Physical Review B* **1991,** *44* (9), 4146-4156.

61. Frenkel, A. I.; Kleifeld, O.; Wasserman, S. R.; Sagi, I. J. T. J. o. c. p., Phase speciation by extended x-ray absorption fine structure spectroscopy. **2002,** *116* (21), 9449-9456.

62. Bernardini, S.; Bellatreccia, F.; Casanova Municchia, A.; Della Ventura, G.; Sodo, A., Raman spectra of natural manganese oxides. *Journal of Raman Spectroscopy* **2019,** *50* (6), 873-888.

63. Post, J. E.; McKeown, D. A.; Heaney, P. J., Raman spectroscopy study of manganese oxides: Tunnel structures. *American Mineralogist* **2020,** *105* (8), 1175-1190.

64. Post, J. E.; McKeown, D. A.; Heaney, P. J., Raman spectroscopy study of manganese oxides: Layer structures. *American Mineralogist* **2021,** *106* (3), 351-366.

65. Rudolph, W. W.; Brooker, M. H.; Tremaine, P. R., Raman spectroscopy of aqueous ZnSO4 solutions under hydrothermal conditions: Solubility, hydrolysis, and sulfate ion pairing. *Journal of Solution Chemistry* **1999,** *28* (5), 621-630.

66. Patel, A. M.; Nørskov, J. K.; Persson, K. A.; Montoya, J. H., Efficient Pourbaix diagrams of many-element compounds. *Physical Chemistry Chemical Physics* **2019,** *21* (45), 25323-25327.

67. Persson, K. A.; Waldwick, B.; Lazic, P.; Ceder, G., Prediction of solid-aqueous equilibria: Scheme to combine first-principles calculations of solids with experimental aqueous states. *Physical Review B* **2012,** *85* (23), 235438.

68. Jain, A.; et al., Commentary: the materials project: a materials genome approach to accelerating materials innovation. *APL Mater.* **2013,** *1*, 11002.

69. Ong, S. P.; Cholia, S.; Jain, A.; Brafman, M.; Gunter, D.; Ceder, G.; Persson, K. A., The Materials Application Programming Interface (API): A simple, flexible and efficient API for materials data based on REpresentational State Transfer (REST) principles. *Computational Materials Science* **2015,** *97*, 209-215.

70. Zhai, X.-Z.; Qu, J.; Hao, S.-M.; Jing, Y.-Q.; Chang, W.; Wang, J.; Li, W.; Abdelkrim, Y.; Yuan, H.; Yu, Z.-Z., Layered Birnessite Cathode with a Displacement/Intercalation Mechanism for High-Performance Aqueous Zinc-Ion Batteries. *Nano-Micro Letters* **2020,** *12* (1), 56.

71. Ko, J. S.; Sassin, M. B.; Parker, J. F.; Rolison, D. R.; Long, Jeffrey W., Combining battery-like and pseudocapacitive charge storage in 3D MnOx@carbon electrode architectures for zinc-ion cells. *Sustainable Energy & Fuels* **2018,** *2* (3), 626-636.